International Journal of Heat and Mass Transfer 217 (2023) 124656

Contents lists available at ScienceDirect

International Journal of Heat and Mass Transfer

journal homepage: www.elsevier.com/locate/ijhmt

BubbleMask: Autonomous visualization of digital flow bubbles for predicting critical heat flux

Sanghyeon Chang [a], Youngjoon Suh [a], Chinmay Shingote [b], Cho-Ning Huang [b], Issam Mudawar [c], Chirag Kharangate [b], Yoonjin Won [a,d,*]

[a] Department of Mechanical and Aerospace Engineering, University of California, Irvine, CA, United States
[b] Department of Mechanical and Aerospace Engineering, Case Western Reserve University, Cleveland, OH, United States
[c] School of Mechanical Engineering, Purdue University, West Lafayette, IN, United States
[d] Department of Electrical Engineering and Computer Science, University of California, Irvine, Irvine, CA, United States

ARTICLE INFO

Keywords:
Flow boiling
Digital bubbles
Microgravity
Computer vision
Autonomous feature extraction

ABSTRACT

Flow boiling utilizes the latent heat of the fluid to provide an efficient thermal management solution through bubble-induced advective transport. In microgravity environments, flow boiling becomes even more advantageous as macroscale flow helps efficiently remove bubbles from the heated wall, resulting in enhancing heat transfer as well as critical heat flux (CHF). However, connecting flow boiling physics and bubble information is a challenging task due to the complexity and high dimensionality of bubble dynamics. To overcome this challenge, the advances in computer vision techniques and models such as VISION-iT can be leveraged to autonomously extract physically meaningful features related to spatial statistics, interfacial characteristics, and bubble dynamics by digitalizing flow bubble information. In this study, 30,000 flow boiling images under microgravity conditions are used to compute ten different features of 155,000 individual bubbles. The extracted bubble information is then used to predict CHF by using a classical flow boiling model, the *Interfacial Lift-off Model*. This vision-based approach suggested here has the potential to revolutionize the study of such thermofluidic topics by providing visual insights that agree well with experimental data.

1. Introduction

Flow boiling is a primary method for thermal management in applications that require the dissipation of large heat loads from small surface areas. Two-phase flow boiling is preferred over single-phase flow because it utilizes the coolant's latent and sensible heat with an enhancement in heat removal [1], resulting in significant enhancement in heat transfer coefficients. However, in heat flux-controlled systems, the advantages are only maintained before the heat flux reaches the upper limit, also known as the critical heat flux (CHF). CHF is a major concern as it can lead to boiling crises, which can interrupt the liquid's access to the heat dissipating. The presence of CHF can trigger unsteady escalation in the wall temperature and eventual catastrophic failure of devices. Therefore, CHF is the one of most important design parameters, which serves as a terminal safety thread for two-phase thermal management systems [2].

Advanced satellites and other space platforms require increased power for these systems. This increase has resulted in a higher demand for effective thermal management and control systems, which in turn rely on two-phase heat transfer [3]. To design reliable and safe heat transport systems for space applications, it is important to understand the differences in vapor behavior between earth and microgravity conditions, particularly with regards to the CHF. In microgravity, bubbles slide along the heated wall and coalesce into larger vapor masses instead of detaching into the bulk flow as in earth gravity conditions. This bubble behavior is primarily driven by liquid inertia that helps to remove the bubbles from the heated wall before they create elongated vapor masses which might act as an insulator [4]. As a result, flow boiling is an efficient thermal management method in microgravity whereas pool boiling is not feasible as it relies on only on gravity-driven bubble detachment. However, the installation of two-phase flow systems has been difficult due to their flow instability and system failure issues associated with CHF. Uncertainty in CHF conditions discourages space system designers from introducing such two-phase systems. Therefore, it is imperative to gain a fundamental understanding and accurately predict CHF in microgravity.

Owing to the complexity and the importance of CHF in the field of

* Corresponding author at: Department of Mechanical and Aerospace Engineering, University of California, Irvine, CA, United States.
E-mail address: won@uci.edu (Y. Won).

https://doi.org/10.1016/j.ijheatmasstransfer.2023.124656
Received 16 May 2023; Received in revised form 8 August 2023; Accepted 28 August 2023
Available online 15 September 2023
0017-9310/© 2023 Elsevier Ltd. All rights reserved.

Nomenclature

A	channel cross-sectional area
b	ratio of wetting front length to wavelength, w/λ
A_g	surface area occupied by the jets
A_w	total surface area
AR	aspect ratio
F	fraction of total heat flux for evaporation
G	mass velocity
G_3	lateral mass velocity
h_{fg}	latent heat of vaporization
i	instance
j	frame
ℓ	interfacial length
q''	wall heat flux
q''_{CHF}	critical heat flux
q''_w	wetting front lift-off heat flux
T	temperature
T_{sat}	saturated temperature
$\Delta T_{sub,in}$	inlet subcooling, $T_{sat,in} - T_{in}$
U	mean velocity
m	number of frames
$\dot{m}$	mass flow rate
N	bubble counts
n	number of instances
v	velocity of bubble
w	wetting front
x	quality

Greek symbols

α	vapor fraction
β_0	y intercept of linear regression
β	regression coefficient
δ	vapor layer thickness
λ	vapor wavelength
λ_c	critical wavelength
ρ_f	density of saturated liquid
ρ_g	density of saturated vapor
σ	surface tension

Subscripts

c	critical
CHF	critical heat flux
f	saturated liquid
g	saturated vapor
in	inlet
ins	instance
loc	local
p	parameters
sat	saturation
sub	subcooled
tot	total
M	sublayer

Superscripts

-	average of total frames

boiling heat transfer, more than a thousand empirical correlations have been developed over the last 60 years to predict CHF values [5]. Researchers have proposed massive experimental verifications and mechanical models based on corresponding experimental results and theoretical reasoning to improve understanding of CHF. Several factors affect CHF, including wettability [6], liquid-spreading ability [7], surface roughness [8], capillarity and wick ability [9], porosity [10,11], Rayleigh-Taylor (RT) instability wavelength [11], and critical pressure [12]. However, the highly complex and interactive mechanism of CHF remains unclear.

There have been suggested models that can predict CHF in microgravity around spatial statistics and interfacial characteristics, but these models require more rigorous validation. One way to validate these models is to use bubble information, but manually extracting bubble information from thousands of images has been difficult. Conventional computer-aided image processing methods such as thresholding (that converts gray-scale images into black-and-white images) or edge detection (that find the boundaries of objects within images by detecting discontinuities in brightness) [13] are ill-suited for heterogenous features like bubbles [14]. In two-phase flows, bubbles show a range of gray color variations due to light reflection instead of appearing monochromatic. Additionally, they do not maintain their spherical shapes as they flow along the channel or cycle through different stages. Flow boiling introduces additional complexity associated with the creation of vapor slugs that travel along the wall, vapor blankets that have thin sublayers below the bubbles, large vapor patches, Helmholtz instability waviness, fluctuations of liquid-vapor interfaces, and intermixing phases. Such uniquely dynamic flow boiling behaviors require the capability to detect and track each moving object within each frame while maintaining their identification numbers to quantify physical descriptors. The key objective of the present study is to identify features related to flow boiling to use them in evaluating CHF values from vision data.

Recent advances in computer vision and deep learning provide a potential for autonomous detection and data curation from visual data. Our group has leveraged these advancements and developed a framework called Vision-Inspired Online Nuclei Tracker (VISION-iT) to extract useful physical descriptors from two-phase heat transfer by digitalizing nucleation-based videos [15,16]. VISION-iT consists of multiple modules based on AI technologies to recognize and track bubbles in a modernized way and record their statistics. Therefore, an optical measurement taken at 2,000 fps with high-speed camera could autonomously translates into rich bubble features that adequately represent the flow boiling system [16–18]. This paradigm shift of two-phase heat transfer allows us to collect physical features and build datasets from transient sequence of imaging. In this paper, we analyze 30,000 images from experimental videos to collect quantitative statistics of 155,000 individual bubbles under ten different microgravity conditions and connect them to a well-known CHF model. The full description of spatial statistics, interfacial characteristics, and bubble dynamics will allow us to identify the most important parameter impacting boiling crisis under microgravity conditions.

2. Theoretical model

Previous significant efforts have demonstrated theoretical models based on feature statistics to explain flow boiling mechanisms, particularly with CHF predictions. Previous CHF mechanism models include *Bubble Crowding Model, Boundary Sublayer Model, Hydrodynamic Instability-based Model*, and *Interfacial Lift-off Model*. Despite the existence of numerous models, it has been challenging to evaluate those models due to the lack of physical features extracted. Along with the advances in computer vision and data science, the capability to autonomously curate millions of informative physical descriptors from boiling images shows the potential for revisiting classical theoretical models from a data-driven perspective.

The *Bubble Crowding Model* [19] describes the formation of a dense

bubbly layer close to the wall at CHF, which renders turbulent fluctuations in the bulk liquid flow. Turbulent fluctuations postulate as the main source of liquid replenishment at the outer edge of the near-wall bubbly layer. As the bubbles become too crowded in the bubbly layer, turbulent fluctuations become too weak to transport liquid towards the wall. The critical heat flux q''_{CHF} can be expressed as:

$$q''_{CHF} = h_{fg} G_3 \frac{(x_2 - x_1)}{F} \tag{1}$$

where h_{fg} is the latent heat of evaporation, G_3 is the lateral mass velocity from the core to the bubble layer due to turbulence, x_1 is the average quality at the core layer, x_2 is the average quality at the bubble layer, and F is the fraction of total heat flux for evaporation. It is critical to understand the contribution of turbulent flow in the bubbly layer.

The *Boundary Sublayer Model* [20] estimates CHF values based on the formation of the vapor blanket and sublayers on the heated wall. The critical heat flux q''_{CHF} can be expressed as:

$$q''_{CHF} = \frac{G_M \delta_M \left(h_{fg} + c_{p,f} \Delta T\right)}{L_M} \tag{2}$$

where G_M is the mass velocity of the sublayer with a micrometer thickness, δ_M is the sublayer thickness, L_M is the length of the vapor blanket or sublayer, and $c_{p,f}$ is the specific heat of the liquid. Therefore, to determine CHF, it is imperative to find the sublayer's parametric relationships to describe the equivalent diameter of the vapor blanket, the length of the vapor blanket or sublayer, mass velocity of the sublayer in addition to fluid properties.

Other representative theoretical models, such as the *Hydrodynamic Instability-based Model* [21,22] *or Interfacial Lift-off Model* [23,24], predict experimental CHF data for both earth gravity and microgravity under various heat integration conditions. In earth gravity conditions, the magnitude of the buoyancy force is highly correlated with vapor removal from the wall and the accumulation of vapor along the heated wall. However, in microgravity conditions, the role of buoyancy becomes negligible due to the absence of the gravity. Without the buoyancy force, vapor accumulates along the wall due to other forces and is pushed in the direction of flow. Therefore, vapor bubbles are observed to coalesce into a wavy vapor layer that propagates along the heated wall prior to CHF. Flow instability is dominated by a balance between surface tension, inertia, and waviness. These theories rely on features such as interfacial instability wavelength (the critical wavelength of vapor waves in the parallel-to-flow direction, as a new bulk liquid is moving in) or Helmholtz instability wavelength (the critical wavelength of vapor waves in the perpendicular-to-wall direction, as liquid continually replenishes evaporating vapor voids), which requires the approximation of instability parameters.

The *Hydrodynamic Instability-based Model* explains the CHF trigger mechanism by combining sub-models, such as Helmholtz instability that calculates the critical wavelength of perpendicular-to-wall liquid-vapor interface, interfacial instability that calculates the critical wavelength of parallel-to-flow vapor wave, and Taylor's interface stability to prevent the liquid from touching the heated surface completely by giving the tendency of CHF [21,22]. Therefore, the critical heat flux q''_{CHF} can be expressed as:

$$q''_{CHF} = \rho_g h_{fg} \frac{\pi}{16} \left(\frac{4\sigma}{\lambda_c}\right)^{1/2} \left[\left(\frac{\rho_f + \rho_g}{\rho_f \rho_g}\right)^{1/2} \Big/ \left(1 + \frac{\rho_g}{\rho_f} \frac{\pi}{16 - \pi}\right) \right] \tag{3}$$

where ρ_g and ρ_f is the density of saturated vapor and liquid, respectively.

The *Interfacial Lift-off Model* is based on the hypothesis that when the momentum of the vapor produced in wetting fronts perpendicular to the wall just exceeds the interface pressure force, the interface will separate from the wall [23,24]. This model consists of sub-models for interfacial instability, mass, momentum and energy conservation, and an interfacial lift-off criterion [25]. By using principles of energy conservation for the vapor and liquid layers, a vapor velocity correlation that relates phase velocities to the average wall heat flux can be obtained. The liquid velocity can be determined using the principle of mass conservation by subtracting the rate of mass conversion to vapor from the total mass flow rate at the channel inlet. The following equation provides predictions of CHF based on the *Interfacial Lift-off Model*:

$$q''_{CHF} = \rho_g \left(c_{p,f} \Delta T_{sub,in} + h_{fg}\right) \left[\frac{4b\pi\sigma \sin(b\pi)}{\rho_g}\right]^{\frac{1}{2}} \delta^{\frac{1}{2}} \Big/ \lambda_c \Big|_{z^*} \tag{4}$$

$c_{p,f}\ \Delta T_{sub,in}$ is the inlet subcooling, h_{fg}, σ is the surface tension, δ is the mean vapor layer thickness, and λ_c is the critical wavelength. z_0 is the stream-wise distance from leading edge of heated wall where $z^* = z_0 + \lambda_c(z^*)$. This means that the combination of bubble or interfacial characteristics, such as mean vapor layer thickness, wavelength, or wetting front as well as flow properties, such as specific heat, latent heat, or surface tension, determines the critical heat flux during flow boiling. The main weakness of the model about its CHF prediction is its reliance on a fixed value of $b = 0.2$ that represents the ratio of the liquid wetting front to the liquid-vapor interfacial wavelength. Taking into account other factors such as working fluid or gravitational force, which can affect the wavelength or wetting front in channel, it cannot be assumed that b values remain constant.

To address this issue, this study leverages a machine learning-assisted framework called VISION-iT, which autonomously captures features from a sequence of images to predict b values. In addition to b, this study also assembles the sets of parameters, such as wavelength or vapor layer thickness, along with new features like interfacial length or velocity, to comprehensively validate the models that predict CHF values.

3. Experimental method

The microgravity flow boiling experimental data used in this study is obtained from Purdue University Boiling and Two-Phase Flow Laboratory's (PU-BTPFL's) experimental database. The specific data used here is based on the microgravity flow boiling facility developed for testing onboard parabolic flights [26,27]. A flow conditioning loop is part of the facility and can provide continuous flow of the FC-72 working fluid to the flow boiling module, allowing for tuning the inlet conditions that were set to provide low subcooling (near-saturated) at the module inlet in the current situation. The flow loop includes a magnetically driven gear pump to circulate the fluid, followed by a filter, a flow meter, and a preheater before entering the flow boiling module. The flow module includes a rectangular channel with a cross-section of 2.5 mm by 5 mm and a heated length of 114.6 mm allowing for single-sided heating on the bottom wall and transparent side walls to provide flow visualization access, enabling the 2D assumption for the vapor volume extraction (Figs. 1a and S2). Exiting the flow boiling module, the two-phase fluid is condensed before being routed through the reservoir back to the pump. A total ten videos are recorded with three mass flow rate ranges from 10 to 40 g/s. Experiments for individual mass flow inlets are conducted for fixed inlet subcooling conditions with heat flux increments until CHF is triggered. Thermocouples are connected along the heated wall to make wall temperature measurements in the fluid to make inlet and outlet fluid temperature measurements. Absolute pressure transducers are connected just upstream and just downstream of the heated section to make fluid pressure measurements. A high-speed camera obtains images in the upstream heated section of the flow boiling module. Each video image is 1.5 s long and is recoded with the frame rate of 2,000 fps, totaling the 3,000 images per case. More details of the experiment and the facility can be found in elsewhere [26,27].

4. Machine learning-assisted analysis

A machine learning-assisted framework, VISION-iT, consists of

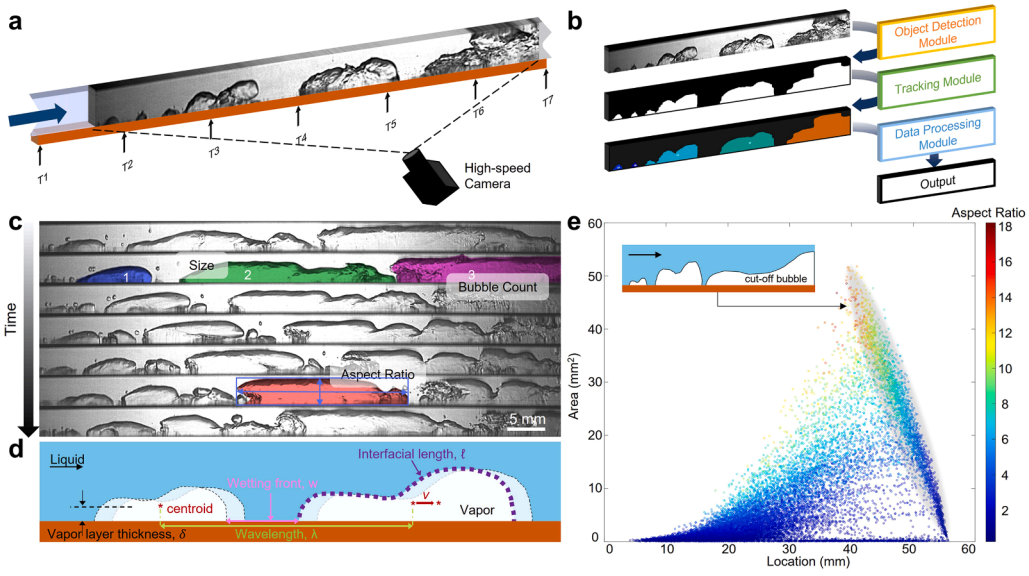

Fig. 1. Vision-based deep learning framework. (a) View of the flow boiling module with key dimensions. High-speed optical images are collected at a framerate of 2,000 fps. (b) The raw images are processed through an object detection module where objects are automatically detected in forms of segmented masks. The masks are then linked and tracked throughout time using a tracking module. The tracked results are then processed using a data processing module to extract physical descriptors based on digital flow bubbles. Schematics are not to scale. (c) The tracking module enables the detection of bubbles with unique IDs for different timestamps. A set of spatial statistics can be obtained to analyze the size, number, and aspect ratio of bubbles, etc. (d) Through data processing module, interfacial characteristics and dynamic characteristics are obtained. (e) The framework enables to analysis all bubbles in sets of 3,000 images. The scatter plot shows both size and aspect ratio of bubbles based on their centroid information. The inset shows an example of a cut-off bubble exiting the channel which results in downward trend in shaded region. These cut-off bubbles are filtered out for further analysis (Figs. 2–6) as they do not depict real shapes.

multiple modules such as object detection, object tracking, and data processing modules to automatically detect and record spatial statistics. The object detection module (Fig. 1b) uses high-resolution flow boiling images and first passes them through a custom-trained instance segmentation model where bubble masks are assigned with unique identifiers (IDs) [16]. This module specifies the type, rough size, and location of objects via bounding box (bbox) regression at this stage, and objects can be entirely segmented from the background with pixel-level accuracy [28,29]. The object tracking module takes the detected masks with linked IDs respect to time and explains in the aspect of spatiotemporal (Fig. 1c). The data processing module post-processes the datasets to filter the indistinguishable objects and extract interfacial and dynamic characteristics (Fig. 1d) [18]. **Supplementary Information (SI)** and our other paper [17] describe more information with steps for detailed instructions on specific machine learning techniques for vision modeling, model evaluation, and data processing modules used for extracting physical parameters where our model is trained with a total of 3,440 images that account for bubbly or wavy-separate regimes under microgravity condition.

5. Results and discussion

5.1. Physically meaningful features

The vision-based framework VISION-iT allows us to extract multi-level, physically meaningful features with in-house algorithms. The features of interest in this study are categorized into spatial statistics, interfacial characteristics, and dynamic characteristics, based on their physical significance, as listed in Table 1.

Table 1
Features of interest regarding flow boiling.

Spatial statistics	Interfacial characteristics	Dynamic characteristics
Counts, size, and aspect ratio.	Wetting front, interfacial length, wavelength, vapor layer thickness, their ratios, and vapor fraction.	Bubble velocity.

Spatial statistics, such as bubble count, size, and aspect ratio, are important to understand flow boiling, as shown in Fig. 1c. In the context of microgravity conditions, bubbles tend to become elongated due to accelerating bubble-bubble connections, resulting in extended bubbles that reach the channel ends. To accurately depict spatial statistics, it is necessary to filter out these extended and cut-off bubbles or floating small bubbles. Additionally, bubbles with rapidly switching identification numbers should also be filtered. Therefore, the plaid patterns in Fig. 2d illustrate the filtered bubbles which are not used in the data analysis in this paper. For the cases of 10, 20, and 40 g/s, 31%, 22%, and 16% of total bubbles are filtered, respectively. The cases of 10 g/s have the largest number of filtered bubbles as lower mass flow rates show most elongated bubbles. It should be noted that the spatial statistics are recorded based on their centroids, meaning that longer bubbles will be located near the location up to 63–82% of the channel. (Fig. 1e), resulting in the peaks in Fig. 2c and f. Beyond this point, data points might not be meaningful.

The *bubble counts N* are recorded during a period of 1.5 s based on $m = 3{,}000$ images with a frame rate of 2,000 , totaling 10,000 to 25,000 bubbles per case. The bubble count per each frame ranges from 3 to 8, depending on the mass flux rates (Fig. 2a). The total bubble counts in Fig. 2d are calculated by accumulating total bubbles in each frame. At higher heat fluxes or lower mass flow rates, larger bubbles are produced, which lead to a decrease in the total number of bubbles.

The bubbles' *size* (Fig. 2b and c) or *aspect ratio AR* (Fig. 2e and f) are indicators of the boiling regimes. At higher heat fluxes or lower mass flow rates, the bubbles tend to coalesce into elongated shapes, resulting in larger bubble sizes up to 80 mm^2 and aspect ratios up to 9. Conversely, larger mass flow rates inhibit bubbles coalescence, resulting in smaller bubble size as small as 0.1 mm^2 and aspect ratio as low as 0.04. Due to the coexistence of small and large bubbles in the channel simultaneously at 10 g/s, the deviations in the bubble sizes are exceptionally high in Fig. 2b.

Flow boiling is complex interfacial phenomena that involves simultaneous interactions between liquid, vapor, and solid phases, resulting in flow instabilities. These *interfacial characteristics* can be characterized by computing the wetting front, interfacial length, their ratios, wavelength, and vapor thickness or fraction from a sequence of images, as

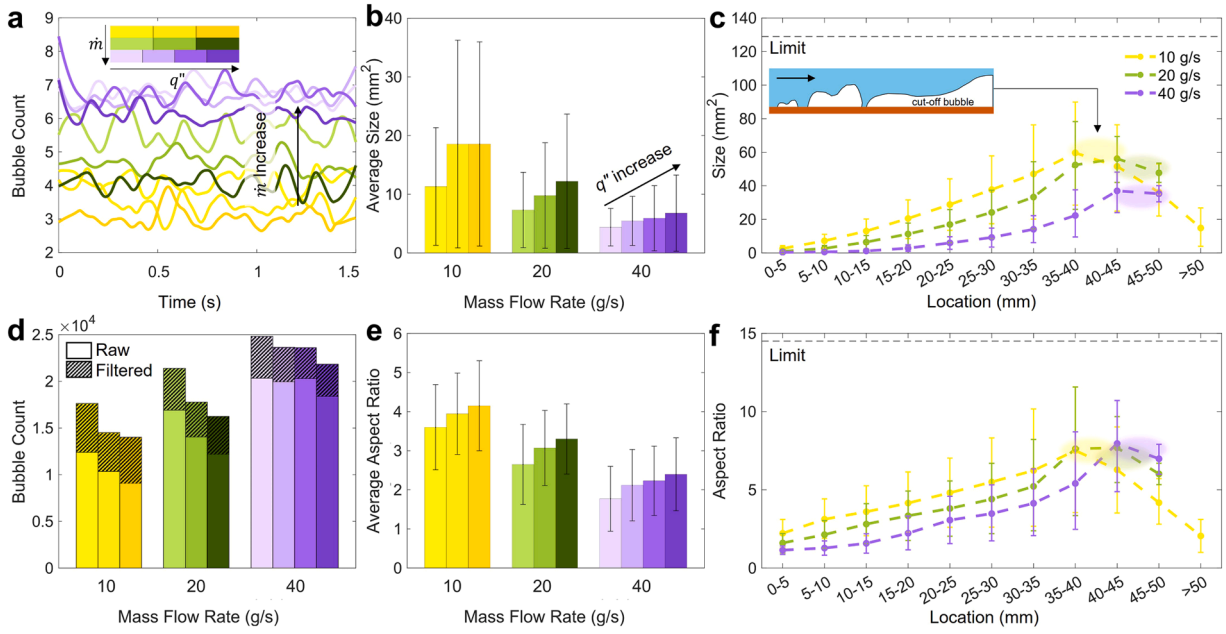

Fig. 2. Spatial statistics. (a) Bubble count per frame with smoothed plot portrays individual bubbles that are identified and counted from 3,000 images of each frame. (b) The average bubble size decreases as the mass flow rate increases, indicating a quantitative competition between bubble growth and removal. (c) The local bubble sizes show an increasing trend until the cut-off point (insert) along the channel. Three lines represent average size of bubbles for each mass flow rate of 10, 20, and 40 g/s. (d) The accumulated total bubble counts from (a) range from 10,000 to 25,000 bubbles. In this study, elongated bubbles that reach the end of channels, cut-off bubbles, are filtered for the size and aspect ratio calculations. Filtered bubbles are represented in a plaid pattern, which is 30–35%, 20–25%, 16–18% for each mass flow rate. After the filtering process, total 155,000 bubbles are used for this study. (e) The average aspect ratio increases as the heat flux increases or the mass flow rate decreases. (f) The local aspect ratio also shows an increasing trend until the cut-off point. All error bars indicate the 16th and 84th percentile of the data set.

illustrated in Fig. 1d.

The *wetting front w*, an interface between the fluid and solid phases, represents a region between discrete vapor bubbles. It plays a key role in providing a continuous access of bulk liquid to the heated wall. The *interfacial length* ℓ, an interface between the fluid and vapor phases, identifies the quantity of liquid molecules that can be potentially evaporated by absorbing heat. Unlike flow boiling in earth gravity conditions, bubbles tend to attach to the bottom surface, which yields smaller wetting fronts and longer interfacial lengths. The wetting front quickly decreases toward end of the channel (Fig. 3a) as bubble-bubble interactions are intensified. In addition, the operating conditions with higher heat fluxes or lower mass rates accelerate bubble growth and merging events, which decreases the wetting front or increases the interfacial length (Fig. 3b and c). The local wetting front length, the average of the total wetting front length, and the average of interfacial length in the channel are calculated by following equations:

$$\overline{w}_{loc} = \frac{1}{n}\left(\sum_{i=1}^{n} w_i\right) \tag{5}$$

$$\overline{w}_{tot} = \frac{1}{m}\sum_{j=1}^{m}\left(\sum_{i=1}^{n} w_i\right) \tag{6}$$

$$\overline{\ell}_{tot} = \frac{1}{m}\sum_{j=1}^{m}\left(\sum_{i=1}^{n} \ell_i\right) \tag{7}$$

where w_i and l_i represent the wetting front and interfacial length for individual instances (e.g., bubbles in this case). In addition, n is the number of instances which could be either within the regime of interest or over the channel, and m is the number of the frames.

The flow visualization shows the vapor layer exhibits fluctuation along the flow direction, which can be represented by the *wavelength* λ that refers to the distance between two obvious wave valleys. The larger mass flow rate accelerates fluctuations, resulting in smaller wavelengths (Fig. 3d). The average of the wavelength for each instance and average of the total wavelength in the channel are given by:

$$\overline{\lambda}_{ins} = \frac{1}{m}\sum_{j=1}^{m}\left(\frac{1}{n}\sum_{i=1}^{n}\lambda_i\right) \tag{8}$$

$$\overline{\lambda}_{tot} = \frac{1}{m}\sum_{j=1}^{m}\left(\sum_{i=1}^{n}\lambda_i\right) \tag{9}$$

where the subscripts *ins* and *tot* refer to the instance-based average and the total summation over the regime of interest.

To compare the interfacial characteristics, the constant b is introduced, which represents the ratio between the wetting front and wavelength. As discussed in the theoretical background section, the value of b is necessary to calculate CHF, as expressed in Eq. (4). However, assuming b to be a constant value of 0.2 for all cases is not practical, as it can vary and increase with higher heat fluxes or lower mass flow rates. In this study, the constant b is extracted from our feature extraction module and ranges from 0.1 to 0.8, as plotted in Fig. 3e and listed in Table 3. The constant b used in this study is calculated:

$$b = \frac{\overline{w}_{tot}}{\overline{\lambda}_{tot}} \tag{10}$$

The *vapor layer thickness* δ is calculated by averaging the bubble height over the channel length, and the *vapor fraction* α is calculated as the ratio of the vapor phase to the total volume. By verifying that assuming spherical bubbles has negligible effects on the total vapor volume calculations, we assume extruded bubble shapes for the simplicity (Fig. S2). The local vapor fraction α_{loc} increases in the flow direction as more vapor is produced at the wall by evaporation and boiling of the liquid sublayer covering the upstream portion of the heater or by boiling in the wetting fronts (Fig. 3g). With higher heat fluxes or lower mass flow rates, the vapor layer thickness or fraction will significantly increase (Fig. 3f and h). Additionally, a vapor fraction at

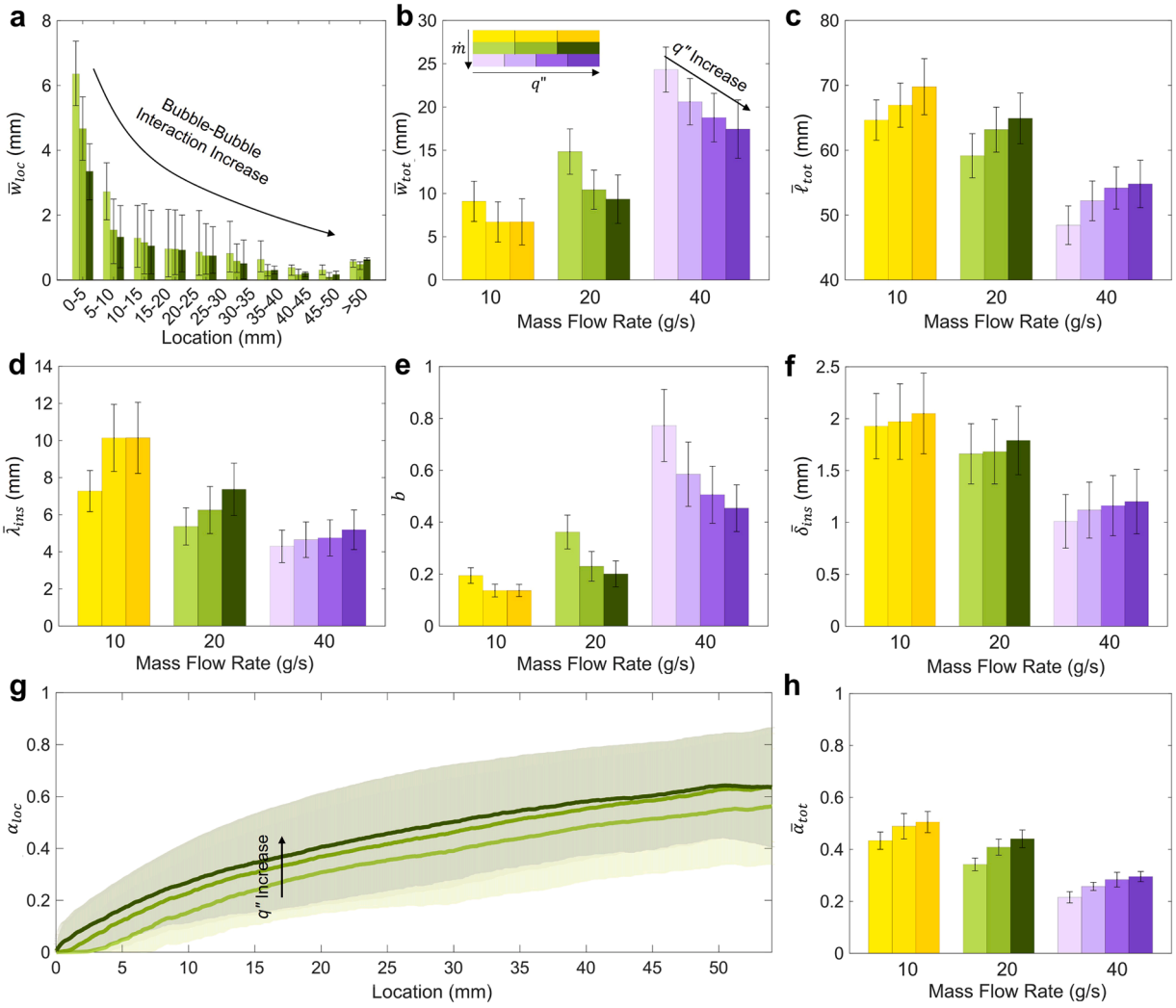

Fig. 3. Interfacial characteristics. (a) Local wetting front $\overline{w}_{loc}$ of a mass flow rate of 20 g/s within the regime of interest. (b) Average of total wetting front over the channel $\overline{w}_{tot}$ for different mass flow rates (10 – 40 g/s) with varying heat flux. (c) Average of total interfacial length $\overline{l}_{tot}$. (d) Average wavelength of individual bubbles $\overline{\lambda}_{ins}$. (e) Constant b representing the ratio of overall wetting front length to overall wavelength. (f) Average vapor layer thickness of individual bubble $\overline{\delta}_{ins}$. (g) Local vapor fraction profile α_{loc} of mass flow rate of 20 g/s. The lines represent average values from 3,000 images, and bands represent one standard deviation for each heat flux. (h) Average of total vapor fraction $\overline{\alpha}_{tot}$. Error bars from (a – d, and f) indicate the 16th and 84th percentile of the data, while error bars in (e) represent one standard deviation.

CHF is shown to be 51%, 44%, and 30% for 10, 20, and 40 g/s, respectively while previous studies postulated that CHF occurs when the vapor fraction exceeds the critical value of 0.82 [20]. The average of vapor layer thickness for each instance, the local vapor fraction, and the average of vapor fraction in the channel can be expressed as:

$$\overline{\delta}_{ins} = \frac{1}{m}\sum_{j=1}^{m}\left(\frac{1}{n}\sum_{i=1}^{n}\left(\frac{\#\ of\ vapor\ pixels\ in\ an\ instance\ i}{length\ of\ instance\ i}\right)_i\right) \tag{11}$$

$$\alpha_{loc} = \left(\frac{\#\ of\ vapor\ pixels}{\#\ of\ liquid\ pixels + vapor\ pixels}\right)_j \tag{12}$$

$$\overline{\alpha}_{tot} = \frac{1}{m}\sum_{j=1}^{m}\left(\frac{\#\ of\ vapor\ pixels}{\#\ of\ liquid\ pixels + vapor\ pixels}\right)_j \tag{13}$$

During flow boiling, liquid and vapor phases flow independently and separately. This is mainly due to the interfacial interactions between different sets of phases, resulting in *bubble dynamics*. For example, forces applied to the bubbles (e.g., drag or adhesion forces, etc.) hinder the bubbles from flowing together with the working fluid. Instead, bubbles tend to flow along the heated wall and coalesce into larger vapor masses before detaching into the bulk flow without buoyancy force conditions [30]. To characterize such phenomena, *bubble velocities* are calculated by measuring the traveling distances of bubble centroids over a certain time period. In Fig. 4a, the average velocities for mass flow rates of 10, 20, and 40 g/s are shown to be 0.5, 0.9, and 1.8 m/s, respectively. These average velocities show the comparable velocities with flow inlet velocity, but the individual bubble velocities vary and increase in the direction of flow in the channel, as described in Fig. 4b. This increasing trend can be attributed to the existence of the bubble-bubble interactions that introduce locally and temporally high velocities. Such interactions are more prominent at lower mass flow rates rather than larger mass flow rates. In SI, we confirm that the individual bubble velocities based on centroid movements of bubbles are comparable with the computed velocities by tracking bubble edges.

5.2. CHF predictions

Interfacial Lift-off Model validation requires the extraction of interfacial characteristics, such as the mean vapor layer thickness δ at the CHF, the critical wavelength λ_c ($=\overline{\lambda}_{ins}$ at CHF) and the ratio of wetting

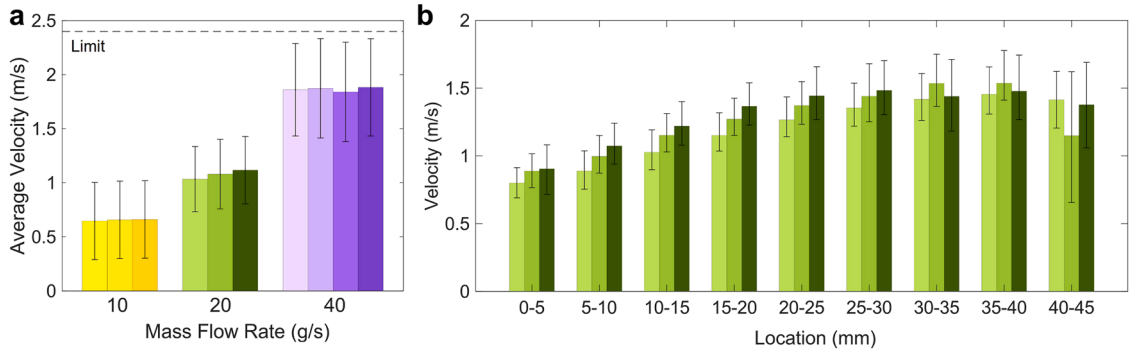

Fig. 4. Bubble dynamics. (a) Average velocity plots for three different mass flow rates (10–40 g/s) with varying heat flux. Each mass flow rate represents 0.5, 0.9 and 1.8 m/s, which is comparable with flow inlet velocity. (b) Local velocity profiles of mass flow rates of 20 g/s within the regime of interest where the other mass flow rates are shown in Fig. S4. Individual bubble velocities increase in the direction of flow in the channel potentially due to bubble-bubble interactions. The filtered bubbles after 45 mm of channel are not depicted in this plot. Both error bars of (a) and (b) indicate the 16th and 84th percentile of the data set for each case.

front length to wavelength *b*. The values listed in Tables 2 and 3 are used to predict CHF values. We hypothesize that acquiring *b* values experimentally, which account for the dynamic nature of evolving interfacial information, can improve the CHF predictions of existing models. A predetermined *b* value of 0.2 is fixed, which infers that the wetting front length is always 20% of the wavelength in CHF conditions. However, the constant *b* should differ based on varying experimental conditions, such as mass flow rate or heat flux. To explore this, we apply varying *b* values computed from the feature extraction in the previous section along with other values listed in Tables 2 and 3, to predict CHF data. Also, it should be noted that Table 3 lists the values of $\overline{\lambda}_{ins}$.

The results presented in Fig. 5a strengthen our hypothesis that considering bubble statistics can reduce the discrepancies between measurement and prediction CHF values. Our prediction achieves 39%, 22%, and 1% error for the mass fluxes of 10, 20, and 40 g/s, respectively. The good agreement of 1% error at 40 g/s can be explained by the use of a more accurate *b* value of 0.46 from the feature extraction. However, the discrepancy between the experimental and theoretical values at 10 and 20 g/s can be explained by the method of data acquisition, which suffers from the viewing window effect. As illustrated in Fig. 5b–d, the viewing window effect describes the difficulty of accurately computing the wavelength of end bubbles, cut-off bubbles, continuous bubbles, or elongated bubbles, which becomes more pronounced at lower mass fluxes. Despite the current state-of-the-art data curation method used here, a significant number of cut-off bubbles (16%–35% of the total bubble numbers) are filtered out during our post-processing, which might affect the accuracy of the computations. To further improve the computation accuracy, increasing the viewing window to physically measure additional bubbles by minimizing the effects of the channel ends can be helpful. Other future work will include improving the post-processing algorithms that can create virtual bubbles beyond the channel ends to enhance the accuracy of constant *b* calculations. These calculations can account for the wavelength for end bubbles, cut-off bubbles, or elongated bubbles.

5.3. Regression analysis

We employ regression analysis to visualize the relationship between multiple explanatory variables and a response variable. Multivariate linear regression (MLR) is one of the simplest and most common machine learning algorithms. It is a mathematical method used for evaluating and quantifying the relationship between the variables considered, allowing for the prediction of their effects. Regression analysis estimates dependent variable '*y*' based on the range of independent variable values '*x*,' as illustrated in Fig. 6a and following equation [31]:

$$y = \beta_0 1 + \beta_1 x_1 + \beta_2 x_2 \cdots \beta_p x_p \tag{14}$$

where β_0 is the y-intercept and β_{1-p} are the regression coefficients that indicate the change in *y* relative to an one-unit change in x_{1-p}.

In the previous section, we demonstrate the capability to quantify ten parameters related to spatial statistics, interfacial characteristics, and bubble dynamics. Therefore, we investigate the importance between individual parameters as explanatory variable values and heat flux or heat transfer coefficient as response variables with an acceptably accurate indication as mean absolute error of $< 3.5 \times 10^{-10}$, as demonstrated in Fig. 6b and c.

The MLR confirms that the wavelength has the highest impact on both heat flux and heat transfer coefficient, which validates the use of wavelength-based analysis for flow boiling under microgravity. The parameters that quantify the vapor such as vapor fraction, constant *b*, and bubble size in addition to bubble velocity also show a high influence compared to the other parameters. It should be noted that the classical *Interfacial Lift-off Model* employs interfacial characteristics that include vapor layer thickness, wavelength, and wetting front. Consequently, it gives an idea that including vapor fraction or other parameters will give another approach to make correlation between the heat flux or heat transfer coefficient. Moreover, as discussed in previous section, our future work needs to consider the viewing window effect to compute parameters accurately which can weight importance differently.

Table 2
Thermophysical properties of FC-72 in experimental condition at CHF.

Mass flow rate (g/s)	T_{sat} (°C)	ρ_g (kg/m^3)	h_{fg} (J/g)	σ (N/m)
10	65.52	17.46	79.17	0.00771
20	65.47	17.46	79.17	0.00771
40	70.24	20.34	79.72	0.00729

Table 3
CHF parameters for validating *Interfacial Lift-off Model*.

Mass flow rate (g/s)	*b*	δ (mm)	λ_c (mm)
10	0.14	2.05	10.14
20	0.20	1.79	7.36
40	0.46	1.20	5.19

6. Conclusion

In this study, a machine learning-assisted framework plays a key role in extracting physically meaningful and quantitative data during flow boiling under microgravity conditions. The framework detects and tracks 155,000 bubbles with high fidelity based on 30,000 optical images, providing sets of parameters such as spatial statistics, interfacial characteristics, and bubble dynamics. These parameters help illustrate

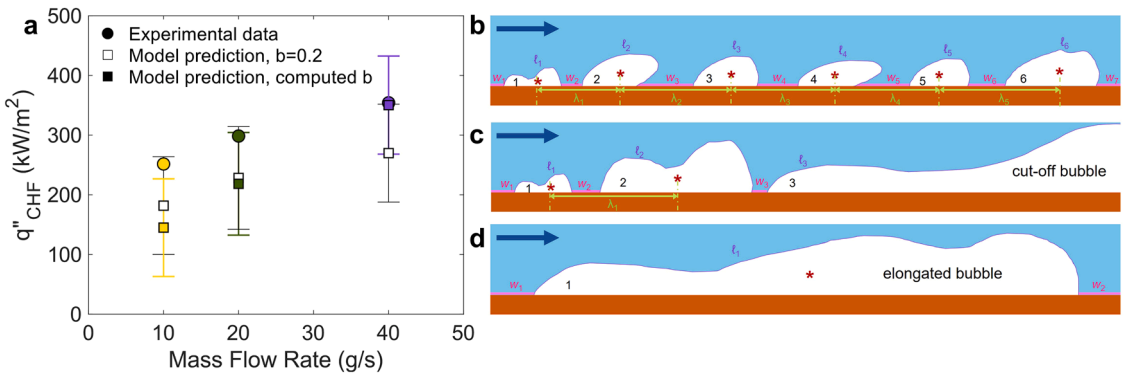

Fig. 5. CHF predictions. (a) Comparison of CHF data measured (circles) and *Interfacial Lift-off Model* predictions with constant (empty square) or computed (solid square) b values. The error bars indicate one standard deviation. The viewing window size works as a constraint and make it difficult to accurately compute the wavelength of (b) end bubbles, (c) cut-off bubbles, continuous bubbles, or (d) elongated bubbles while other interfacial characteristics (e.g., interfacial length ⁄) are preserved and included in the calculation.

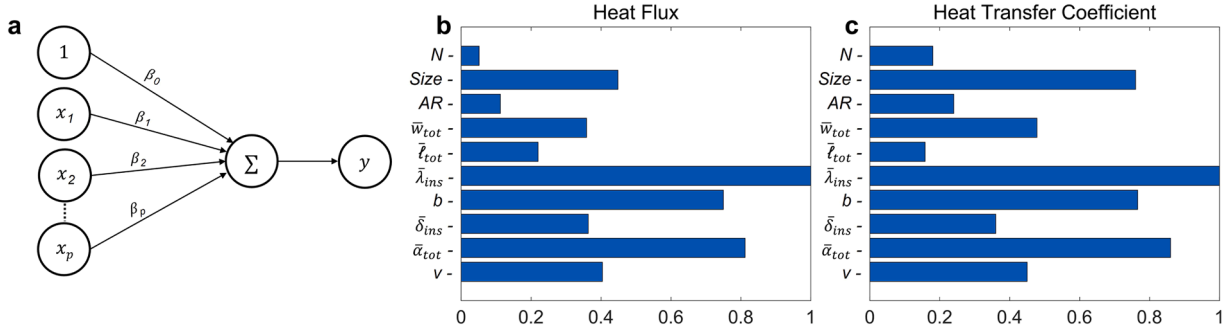

Fig. 6. Multivariate linear regression with heat flux and heat transfer coefficient for flow boiling data set. (a) Multivariate linear regression using the weighted sum of input features (independent variables) to estimated output (dependent variable). Values of importance between explanatory variable values and response parameters such as (b) heat flux and (c) heat transfer coefficient are normalized.

the relationships between operating conditions, such as mass flow rate or heat flux, and their effects of hindering or merging events in the perspective of bubbles. Based on the bubble information derived from the framework, the effectiveness of the *Interfacial Lift-off Model* under microgravity conditions is evaluated in this study. The model predictions show errors of 39%, 22%, and 1% for 10, 20, and 40 g/s, respectively. While the results demonstrated good agreement, particularly for larger mass flow rates, discrepancies between experimental and prediction values at lower mass flow rates can be attributed to two limitation factors: a viewing window effect and the intrinsic transient nature of bubble dynamics. Classical CHF prediction models heavily rely on parameters such as spatial statistics of individual instances or interfacial characteristics. However, current meaturement methodology makes it challenging to accurately quantify the actual length scales of bubbles in a lengthy channel (due to the distortion at the edge and measurement angles), and capture continuous bubble appearances (e.g., elongated and/or cut-off bubbles). This motivates not only high-fidelty measurement efforts that minimize window effects but also modeling efforts that can overcome these limitations by generating the views beyond the scenes to observe holistic flow structures. Furthermore, classical models infer transient and dynamic CHF phenomena using static images instead of sequences of images or videos, failing to capture dynamic bubble characteristics such as explosive growth of vapor bubbles, flow instability, or bubble-bubble interactions. These limitations highlight the need for a new approach that can capture transient and dynamic bubble phenomena.

CRediT authorship contribution statement

Sanghyeon Chang: Conceptualization, Methodology, Validation, Writing – original draft. **Youngjoon Suh:** Conceptualization, Methodology, Writing – review & editing. **Chinmay Shingote:** Resources. **Cho-Ning Huang:** Resources. **Issam Mudawar:** Resources, Writing – review & editing. **Chirag Kharangate:** Resources, Writing – review & editing. **Yoonjin Won:** Supervision, Writing – review & editing.

Declaration of Competing Interest

The authors declare the following financial interests/personal relationships which may be considered as potential competing interests:

Yoonjin Won reports financial support was provided by Office of Naval Research. Chirag Kharangate reports financial support was provided by Office of Naval Research.

Data availability

The authors do not have permission to share data.

Acknowledgments

This work was sponsored by the Office of Naval Research (ONR) with Dr. Mark Spector under Grant No. N00014-22-1-2063. This work was also partially sponsored by the Office of Naval Research (ONR) under Grant No. N00014-21-1-2078. The authors thank Purdue University Boiling and Two-Phase Flow Laboratory (PU-BTPFL) for sharing experimental data that was used for investigating the AI vision models developed in this study.

Supplementary materials

Supplementary material associated with this article can be found, in the online version, at doi:10.1016/j.ijheatmasstransfer.2023.124656.

References

[1] C.R. Kharangate, L.E. O'Neill, I. Mudawar, M.M. Hasan, H.K. Nahra, R. Balasubramaniam, R. Balasubramaniam, N. Hall, A. Macner, J. Mackey, Flow boiling and critical heat flux in horizontal channel with one-sided and double-sided heating, Int. J. Heat Mass Transf. 90 (2015) 323–338.

[2] Mudawar I. Two-phase microchannel heat sinks: theory, applications, and limitations. 2011.

[3] J.P. Hartnett, T.F. Irvine, G.A. Greene, Y.I. Cho, Advances in Heat Transfer, Academic Press, 1998.

[4] H. Zhang, I. Mudawar, M.M. Hasan, Flow boiling CHF in microgravity, Int. J. Heat Mass Transf. 48 (15) (2005) 3107–3118.

[5] S. Xie, M.S. Beni, J. Cai, J. Zhao, Review of critical-heat-flux enhancement methods, Int. J. Heat Mass Transf. 122 (2018) 275–289.

[6] S.J. Kim, I.C. Bang, J. Buongiorno, L.W. Hu, Effects of nanoparticle deposition on surface wettability influencing boiling heat transfer in nanofluids, Appl. Phys. Lett. 89 (15) (2006), 153107.

[7] H. O'Hanley, C. Coyle, J. Buongiorno, T. McKrell, L.W. Hu, M. Rubner, R. Cohen, Separate effects of surface roughness, wettability, and porosity on the boiling critical heat flux, Appl. Phys. Lett. 103 (2) (2013), 024102.

[8] K.H. Chu, Y. Soo Joung, R. Enright, C.R. Buie, E.N. Wang, Hierarchically structured surfaces for boiling critical heat flux enhancement, Appl. Phys. Lett. 102 (15) (2013), 151602.

[9] H.D. Kim, M.H. Kim, Effect of nanoparticle deposition on capillary wicking that influences the critical heat flux in nanofluids, Appl. Phys. Lett. 91 (1) (2007), 014104.

[10] M.M. Rahman, E. Olceroglu, M. McCarthy, Role of wickability on the critical heat flux of structured superhydrophilic surfaces, Langmuir 30 (37) (2014) 11225–11234.

[11] A. Nazari, S. Saedodin, Critical heat flux enhancement of pool boiling using a porous nanostructured coating, Exp. Heat Transf. 30 (4) (2017) 316–327.

[12] L. Tan, C. Chen, X. Dong, Z. Gong, M. Wang, Experimental study on CHF of R134a flow boiling in a horizontal helically-coiled tube near the critical pressure, Exp. Therm Fluid Sci. 82 (2017) 472–481.

[13] Y.J. Kim, J.Y. Lee, Algorithm of a perspective transform-based PDF417 barcode recognition, Wirel. Pers. Commun. 89 (2016) 893–911.

[14] M.T. Hughes, G. Kini, S. Garimella, Status, challenges, and potential for machine learning in understanding and applying heat transfer phenomena, J. Heat Transf. 143 (12) (2021) 4–7.

[15] J. Lee, Y. Suh, P.P. Dubey, M.T. Barako, Y. Won, Capillary wicking in hierarchically textured copper nanowire arrays, ACS Appl. Mater. Interfaces 11 (1) (2018) 1546–1554.

[16] Y. Suh, J. Lee, P. Simadiris, X. Yan, S. Sett, L. Li, K. Rabbi, N. Miljkovic, Y. Won, A deep learning perspective on dropwise condensation, Adv. Sci. 8 (22) (2021), 2101794.

[17] Suh Y., Chang S., Simadiris P., Inouye T., Hoque M., Khodakarami S., Kharangate C., Miljkovic N., Won Y. VISION-iT: deep nuclei tracking framework for digitalizing bubbles and droplets, *Submitted*. 2023. https://papers.ssrn.com/sol3/papers.cfm?abstract_id=4491956.

[18] Y. Suh, R. Bostanabad, Y. Won, Deep learning predicts boiling heat transfer, Sci. Rep. 11 (1) (2021) 1–10.

[19] J. Weisman, B.S. Pei, Prediction of critical heat flux in flow boiling at low qualities, Int. J. Heat Mass Transf. 26 (10) (1983) 1463–1477.

[20] C.H. Lee, I. Mudawar, A mechanistic critical heat flux model for subcooled flow boiling based on local bulk flow conditions, Int. J. Multiph. Flow 14 (6) (1988) 711–728.

[21] C.N. Huang, C.R. Kharangate, Consolidated model for predicting flow boiling critical heat flux in single-sided and double-sided heated rectangular channels, Int. J. Heat Mass Transf. 160 (2020), 120132.

[22] C.N. Huang, C.R. Kharangate, A new mechanistic model for predicting flow boiling critical heat flux based on hydrodynamic instabilities, Int. J. Heat Mass Transf. 138 (2019) 1295–1309.

[23] J.E. Galloway, I. Mudawar, CHF mechanism in flow boiling from a short heated wall-part 1. Examination of near-wall conditions with the aid of photomicrography and high-speed video imaging, Int. J. Heat Mass Transf. 36 (1993) 2511–2526.

[24] J.E. Galloway, I. Mudawar, CHF mechanism in flow boiling from a short heated wall—II. Theoretical CHF model, Int. J. Heat Mass Transf. 36 (10) (1993) 2527–2540.

[25] H. Zhang, I. Mudawar, M.M. Hasan, Experimental and theoretical study of orientation effects on flow boiling CHF, Int. J. Heat Mass Transf. 45 (22) (2002) 4463–4477.

[26] C. Konishi, H. Lee, I. Mudawar, M.M. Hasan, H.K. Nahra, N.R. Hall, J. Wagner, R. May, J. Mackey, Flow boiling in microgravity: part 1–Interfacial behavior and experimental heat transfer results, Int. J. Heat Mass Transf. 81 (2015) 705–720.

[27] C. Konishi, H. Lee, I. Mudawar, M.M. Hasan, H.K. Nahra, N.R. Hall, J. Wagner, R. May, J. Mackey, Flow boiling in microgravity: part 2–critical heat flux interfacial behavior, experimental data, and model, Int. J. Heat Mass Transf. 81 (2015) 721–736.

[28] S. Ren, K. He, R. Girshick, J. Sun, Faster r-cnn: towards real-time object detection with region proposal networks, Adv. Neural. Inf. Process Syst. 28 (2015).

[29] S. Khodakarami, K.F. Rabbi, Y. Suh, Y. Won, N. Miljkovic, Machine learning enabled condensation heat transfer measurement, Int. J. Heat Mass Transf. 194 (2022), 123016.

[30] Cochran T.H. Forced-convection boiling near inception in zero gravity. National Aeronautics and Space Administration; 1970.

[31] G.A.F. Seber, A.J. Lee, Linear Regression Analysis, 330, John Wiley & Sons, 2003.